Vacuum 202 (2022) 111165

Contents lists available at ScienceDirect

Vacuum

journal homepage: www.elsevier.com/locate/vacuum

Etching characteristics of low-*k* SiCOH thin films under fluorocarbon-based plasmas

Jacob Comeaux [a,1], William Wirth [a,1], Justin Courville [a], Nam-Wuk Baek [b], Donggeun Jung [b], Seonhee Jang [a,*]

[a] Department of Mechanical Engineering, University of Louisiana at Lafayette, Lafayette, LA, 70503, USA
[b] Department of Physics, Sungkyunkwan University, Suwon, 16419, South Korea

ARTICLE INFO

Keywords:
Plasma enhanced chemical vapor deposition
Low-*k*
SiCOH
Reactive ion etching
Fluorocarbon

ABSTRACT

Low dielectric constant (low-*k*) SiCOH thin films were prepared on silicon (Si) wafers using plasma enhanced chemical vapor deposition (PECVD) of the precursor tetrakis(trimethylsilyloxy)silane (TTMSS). The deposition RF plasma power was 20 and 100 W. The *k*-values were 2.14 and 3.2 for the films deposited at 20 and 100 W, respectively. The deposited films then underwent an inductively coupled plasma-reactive ion etching (ICP-RIE) using fluorocarbon-based etching gas of CF_4, CF_4+O_2, and CF_4+Ar. After etching, the etch rate and refractive index for the films deposited at 100 W were higher than those at 20 W. The surface roughness decreased for the films at 20 W but increased for those at 100 W after etching. Contact angles decreased indicating a hydrophilic surface after etching. Prominent absorption bands from the Fourier transform infrared (FTIR) spectra were observed as C–H_x stretching, Si–CH_3 bending, Si–O–Si stretching, and Si–$(CH_3)_x$ bending vibration modes. X-ray photoelectron spectroscopy (XPS) showed a significant fluorine concentration on the film surface. From high resolution scans for C1s and F1s in the XPS, dominant peaks were observed as C–H/C–C and C–F_3 after etching, respectively. After etching, the *k*-values and leakage current densities increased from those of as-deposited films.

1. Introduction

As semiconductor devices get smaller and components become closer together, one issue that arises is the resistance-capacitance (RC) delay in the interconnects, resulting in the degradation in the performance of devices [1,2]. To reduce the resistance, aluminum (Al) has been replaced by copper (Cu) because the resistivity of Cu (1.68 μΩ·cm) is smaller than that of Al (2.65 μΩ·cm). To decrease the capacitance, a low dielectric constant (low-*k*, $k < 4.0$) has been employed in place of traditional SiO_2 ($k = 4.2$) for the intermetal dielectric (IMD) material. As low-*k* materials, carbon doped silicon oxide materials, also called SiCOH, have been introduced [3,4]. The low-*k* materials are generally formed by co-deposition of two precursors with a combination of a silica-like matrix precursor and a sacrificial organic polymer (so-called porogen) precursor, followed by UV or thermal curing process. This is the most common process to produce porosity in the film which contributes to low-*k* values. The precise control of deposition conditions as well as the type of precursor molecules have an effect on formation of porosity in the film [5,6]. Some studies have used a single precursor to create low-*k*, SiCOH thin films eliminating the need for a sacrificial porogen [7,8]. In an integrated circuit (IC) chip manufacturing, the interconnects integration requires the dielectric patterning followed by metal (Cu) filling, and chemical-mechanical polishing (CMP), so-called "damascene" process [9]. Dry etching of Cu is very challenging because it is difficult to remove non-volatile by-products such as chlorides or fluorides. Thus, the dielectric patterning has been adopted to avoid Cu patterning. This brought the need for low-*k* dielectric patterning by plasma etching.

There are some barriers in etching of low-*k* materials due to their low density and porous structure including hard mask selectivity and plasma induced damage [10,11]. The mechanism for plasma induced damage can be both physical and chemical which is influenced by various factors including ion bombardment, deep vacuum ultraviolet (VUV) interaction and chemical reactions between radicals and the film [12,13]. Fluorine damage, namely fluorination and implantation have been found to have adverse effects on electrical and chemical properties of the film [14].

* Corresponding author.
E-mail address: seonhee.jang@louisiana.edu (S. Jang).
[1] These authors contributed equally to this work.

https://doi.org/10.1016/j.vacuum.2022.111165
Received 17 December 2021; Received in revised form 7 May 2022; Accepted 8 May 2022
Available online 20 May 2022

Less polymerizing fluorocarbon plasma has caused the greatest damage to SiCOH films [15]. It has been known that etching mechanisms in fluorocarbon plasmas is dictated by processes in the fluorocarbon layer formed on the surface of the film during etching [16–19]. Additionally, the formation of Si–OH bonds caused by fluorine radicals during etching results in the film becoming hydrophilic. Moisture absorbtion in the film can degrade film reliability and result in a higher *k*-value [20–22]. Therefore, the wettability of the film is of importance. Because of the various etching steps in dual damascene processing, various plasma additives need to be studied.

Oxygen (O_2) is often combined with fluorocarbon gases to lessen polymerization on the surface and increase the yield of fluorine (F) atoms [23,24]. A small addition of O_2 to fluorocarbon gas can significantly increase the etch rate but can also be damaging to porous, low-*k* materials [25–28]. Film damage is induced by O_2 plasma processing through changes in chemical bonding by the removal of Si–CH_3 bonds [29]. Because of this, etching parameters with O_2 gas should be fine tuned to minimize damage to the low-*k* material. Additionally, argon (Ar) gas is often introduced with fluorocarbon gases as a dilutant. It has been found that Ar ion bombardment enhances surface reactions therefore enhancing the dissociation of the fluorocarbon gas [30]. Despite its benefits, an increase of VUV-damage in the film has been linked to Ar dilutance in fluorocarbon plasma requiring further research [31]. For successful implementation of the low-*k* patterning, it is crucial to characterize and understand the low-*k* material's performance under various dry etching processes.

In this study, low-*k* SiCOH thin films were prepared by plasma enhanced chemical vapor deposition (PECVD) of a single precursor of tetrakis(trimethylsilyloxy)silane (TTMSS, $C_{12}H_{36}O_4Si_5$) at different plasma powers, yielding the films with varying material properties. Then, an inductively coupled plasma-reactive ion etching (ICP-RIE) was performed to investigate the etching characteristics of the low-*k* SiCOH thin films. Fluorocarbon (CF_4)-based etching chemistry was selected among CF_4, CF_4+O_2, and CF_4+Ar gases. Etch rate and refractive index were determined by deposition conditions and etching parameters. Surface roughness and hydrophilicity of the film were observed depending on etching gas combinations. The chemical structure and elemental composition of the as-deposited film were compared with those of the film after etching. Electrical properties including the *k*-values and leakage current densities were analyzed to examine the electrical stability after etching.

2. Experimental

The SiCOH thin films were deposited by PECVD with the TTMSS (Sigma Aldrich, 97% purity) precursor. The TTMSS precursor is made up of a Si–O cross-shaped structure containing a central silicon atom bonded to four oxygen atoms. Each of the four oxygen atoms are attached to one silicon atom bonded to three methyl groups. This molecular structure of the precursor is expected to improve cross-linking in the film during deposition. Highly boron-doped p^{++}-type Si (100) wafers with a resistivity of 0.001–0.005 Ω-cm were used as substrates. Si wafers were cleaned prior to the deposition process via an ultrasonic cleaning in acetone and ethanol, each for 5 min, followed by three rinses in deionized water. When the substrate was placed on the susceptor in a reactor, additional substrate cleaning was performed using Ar plasma generated at a radio frequency (RF) of 13.56 MHz. Ar gas with a purity of 99.999% was carried into the reactor to generate the plasma at 50 W for 3 min. After Ar plasma cleaning, the deposition of SiCOH thin film was conducted. To vaporize the molecules from the liquid precursor effectively, the bubbler containing the TTMSS precursor was heated to 85 °C. Ar gas was then used as a carrier gas which transports the vaporized precursor molecules from the bubbler to the reactor. The films were deposited at room temperature at an operating pressure of 26.7 Pa. The flow rate of Ar gas flowing through the bubbler was maintained at 18 sccm. The RF plasma power with 13.56 MHz was chosen as 20 and 100 W for deposition, respectively.

The ICP-RIE processes were performed on the as-deposited SiCOH thin films using an Oxford ICP-DRIE System 100 ICP180. Before each etching process, O_2 plasma cleaning was conducted on a bare silicon wafer for 30 s to ensure reproducible etching condition. Then, as-deposited SiCOH films were loaded in the process chamber. Etching gases were selected from CF_4, CF_4+O_2, and CF_4+Ar. The flow rate of CF_4 was fixed at 35 sccm and O_2 and Ar were added with flow rates of 24 sccm, respectively. The RF power was maintained at 200 W at 13.56 MHz and the ICP power at 40 W. The operating pressure was kept constant at 10.0 Pa. The temperature was maintained at room temperature (25 °C). Each etching process was conducted for 30 s.

Thickness and refractive index of as-deposited and etched SiCOH thin films were measured using ellipsometer (alpha-SE, J.A. Woollam) at a wavelength of 633 nm. Etch rates of the films were calculated by the difference in thicknesses after etching for a given time. Surface roughness and contact angle of the films were measured with atomic force microscope (AFM, SmartSPM, Horiba) and contact angle goniometer (Ossila), respectively. Elemental mapping was conducted to identify the distribution of constituent elements using an ultra-high-resolution analytical scanning electron microscopy (SEM, Scios 2 DualBeam, Thermo Fisher Scientific) with an acceleration voltage of 5 kV and mapping resolution of 512 × 340, and with an energy dispersive spectroscope (EDS) detector (UltraDry 100 M, Thermo Fisher Scientific). The chemical structure of the films was investigated by Fourier transform infrared (FTIR) spectroscopy and X-ray photoelectron spectroscopy (XPS) analyses. FTIR (Invenio-S, Bruker) with a Vari GATR attachment was scanned 64 times in the wavenumber range of 4000–600 cm^{-1} at a resolution of 4 cm^{-1}. The chemical compositions of the SiCOH films were analyzed using XPS (ESCA 2SR, ScientaOmicron) with a mono Al Kα X-ray source (1486.6 eV) at an electron emission angle of 90° with a circular analysis area of 1.93 mm in diameter. A scanning step of 0.1 eV with the survey scan range of 0–1200 eV was used. A charge neutralizer was used during analysis. Chamber pressure was maintained below 4 × 10^{-7} Pa. High resolution scans for Si2p, C1s, O1s, and F1s were also collected. In the XPS system, an ion source FDG 150 was used to sputter the samples by Ar ion at 4000 eV and incident angle of 45°. XPS analysis was performed before and after Ar sputtering for 2 min to compare the elemental composition changes throughout the film. In the XPS analysis, although the calibration was conducted using C1s (C–C/C–H, 284.8 eV) as used in other research groups [32–39], it should be noted that the highest degree of caution is required in analysis of the results. Adventitious carbon is generally unknown compound and may not be an inherent part of the film. Alternative calibration methods have been found in recent literatures [40–42]. It has been suggested that the C1s calibration could be replaced by the alternative methods, considering the measurement of the density of states close to the Fermi level followed by the usage of the Fermi edges as the energy reference or the utilization of the work function measured by ultraviolet photoelectron spectroscopy [40–42]. Constituent peaks in FTIR and XPS spectra were identified by the deconvolution using the Gaussian peak fitting from OriginPro and CasaXPS software, respectively. XPS peak fitting in CasaXPS utilized the Shirley background method and the Gaussian-Lorentzian line shapes for peak fitting. The full width at half maximum (FWHM) and peak position of each curve were unconstrained during fitting. To determine I–V/C–V characteristics, a metal-insulator-silicon (MIS, Al/SiCOH/Si) structure was created by deposition of Al dots on the thin films by electron beam evaporation. The *k*-values were obtained from the measured capacitances using RF LCR meter (J4287A, Agilent) conducted at a frequency of 1 MHz. The leakage currents were measured using an electrometer (6517B, Keithley). Elastic modulus (E) and hardness (H) were measured using nano-indentation (Nano Indenter G200, KLA) with continuous stiffness measurement (CSM) mode.

Table 1
Material properties of as-deposited SiCOH thin films.

Plasma power (W)	Dielectric constant (k)	Contact angle (deg.)	Surface roughness (nm)	Refractive index	Elastic modulus (GPa)	Hardness (GPa)
20	2.14	106.4	0.49	1.448	1.24	0.05
100	3.2	102.8	0.39	1.512	18.5	3.02

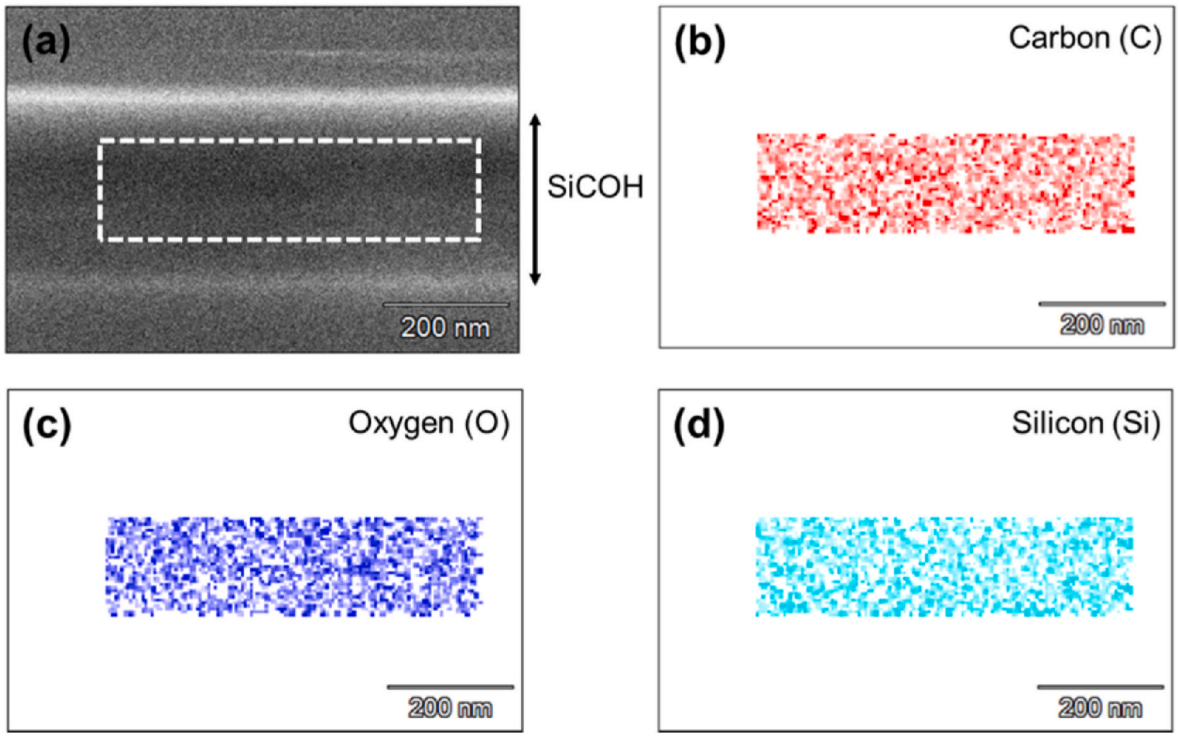

Fig. 1. (a) SEM cross-section image of the SiCOH film at 20 W and its elemental mapping for (b) carbon, (c) oxygen, and (d) silicon from the rectangle region in (a).

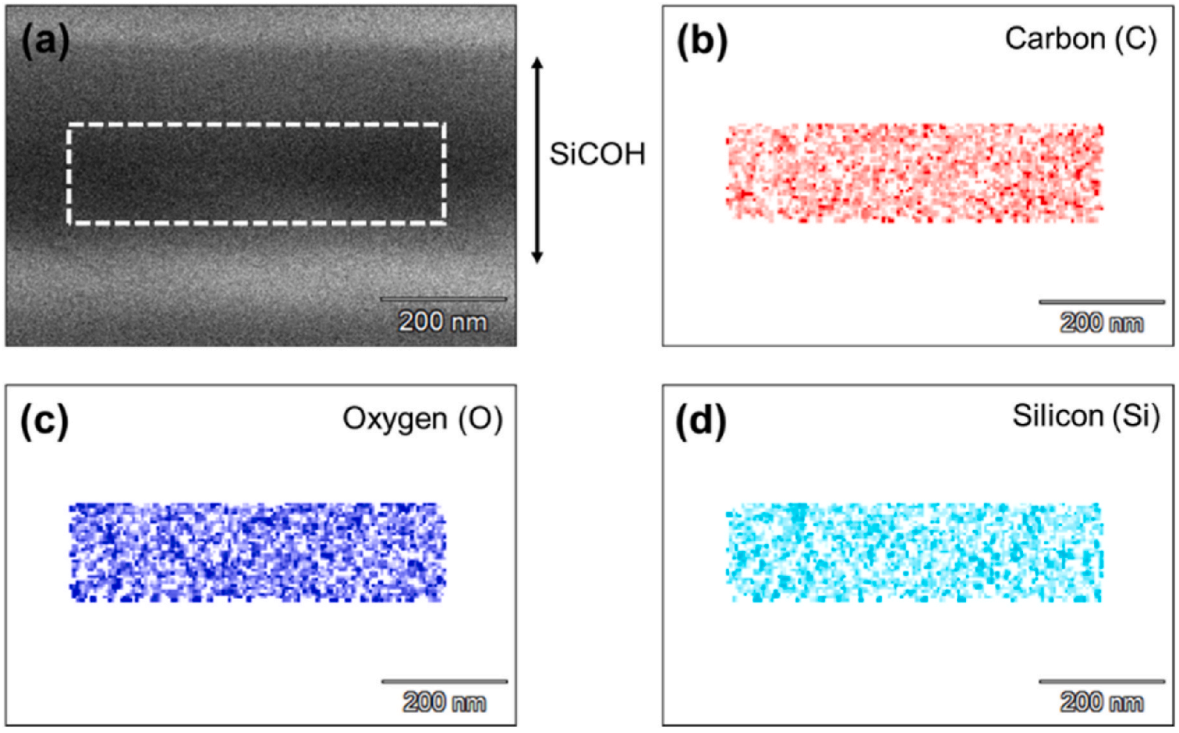

Fig. 2. (a) SEM cross-section image of the SiCOH film at 100 W and its elemental mapping for (b) carbon, (c) oxygen, and (d) silicon from the rectangle region in (a).

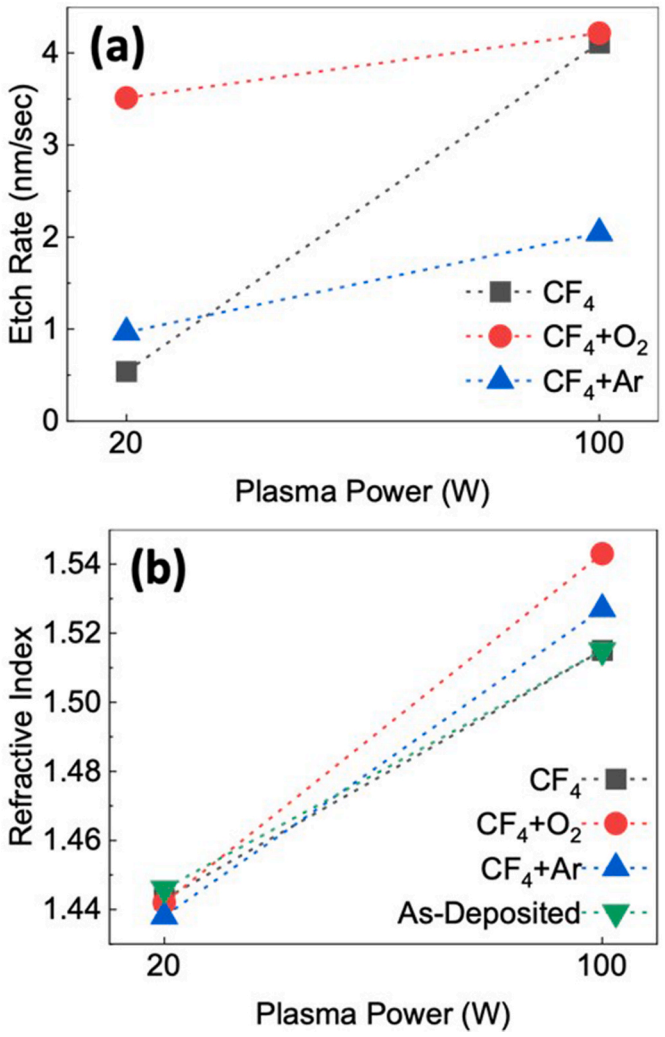

Fig. 3. (a) Etch rate and (b) refractive index of etched SiCOH thin films using etching gases of CF_4, CF_4+O_2, and CF_4+Ar for deposition plasma powers of 20 and 100 W.

3. Results and discussion

3.1. Properties of as-deposited SiCOH thin films

Table 1 presents the properties of as-deposited SiCOH thin films with the deposition plasma powers of 20 and 100 W. The average *k*-values of the films deposited at 20 and 100 W were 2.14 and 3.20, respectively. Contact angles were measured as 106.4 and 102.8° for the films at 20 and 100 W, respectively. The film deposited at 20 W showed more hydrophobicity. Surface roughness was calculated by the root mean square (RMS), measuring the average of surface heights and depths across the surface. The RMS (0.49 nm) of the film deposited at 20 W was higher than that (0.39 nm) of the film at 100 W. Refractive indices were obtained as 1.448 and 1.512 for the films at 20 and 100 W, respectively. The *k*-value and refractive index of the film at 20 W were smaller than those of the film at 100 W. Elastic modulus and hardness of the film at 100 W were measured as 18.5 and 3.02 GPa, respectively, which were higher than those at 20 W. Two SiCOH films deposited at different plasma power, having different material properties, were used to assess etching characteristics.

Fig. 1(a) presents the SEM cross-section image of the SiCOH film deposited at 20 W. By taking the rectangle region of the film in Fig. 1(a), elemental mapping was conducted for carbon, oxygen, and silicon as a result of EDS analysis as shown in Fig. 1(b)–(c), respectively. All elements were evenly distributed throughout the cross-section. There were no segregation or clusters formed in the film. Atomic percentages were obtained as 29.92, 34.03, and 36.06 atomic % for their respective C, O, and Si elements.

Fig. 2(a) presents the SEM cross-section image of the SiCOH film deposited at 100 W. From the elemental mapping from the rectangle region of the film in Fig. 2(a), carbon, oxygen, and silicon were uniformly distributed throughout the cross-section as shown in Fig. 2(b)–(c), respectively. Like the mapping for the film deposited at 20 W, there were no segregation or clusters formed in the film. Atomic percentages were obtained as 26.85, 40.17, and 32.99 atomic % for their respective C, O, and Si elements. In comparison to the film at 20 W, lower carbon and silicon concentrations were measured while higher oxygen concentration was obtained.

3.2. Etch rate and refractive index

Fig. 3 (a) presents the etch rate of the SiCOH films etched with various fluorocarbon combinations including CF_4, CF_4+O_2, and CF_4+Ar for the deposition plasma powers of 20 and 100 W. SiCOH materials required F-based etching chemistry because silicon can be removed by forming volatile SiF_x compounds by the reaction between silicon and fluorine. Fluorine also removes carbon by forming volatile fluorocarbon. Ion bombardments contribute to breaking the Si–O and Si–C bonds in etching process. All films deposited at 100 W showed an increased etch rate from the films deposited at 20 W for all etching conditions. It should be noted that the as-deposited film at 20 W had a lower *k*-value and lower elastic modulus and hardness than the film at 100 W, indicating a lower density in the film at 20 W. Interestingly, a higher etch rate was observed for the denser film at 100 W. Etching in a sole CF_4 gas produced a significantly higher etch rate of 4.1 nm/s for the film at 100 W, compared to 0.539 nm/s for the film at 20 W. For etching in CF_4+O_2, both films deposited at 20 and 100 W exhibited the highest etch rate at 3.5 and 4.2 nm/s. This can be contributed to oxygen's interaction with CF_x radicals, causing an increase in CF_4 dissociation leading to higher concentrations of CF_x radicals therefore increasing the etch rate [23,43]. It was reported that an addition of oxygen can cause the drastic increase in the etch rate and oxygen radicals may damage low-*k* materials especially if they are highly porous [20]. Highly reactive oxygen atoms diffuse through the film breaking up Si–CH_3 bonds and forming hydrophilic Si–OH terminal bonds [44,45]. For etching in CF_4+Ar, the etch rate (2.043 nm/s) of the film deposited at 100 W was higher than that (0.96 nm/s) of the film at 20 W. The prominent etching mechanism in Ar plasma is ion bombardment [46]. Ion bombardments are one of the factors to increase the etch rate. The etch rate slightly increased when Ar was added to CF_4 for the film at 20 W. The etch rate for CF_4+Ar didn't increase much compared to CF_4 or CF_4+O_2. From Table 1, the film at 100 W showed higher elastic modulus (18.5 GPa) and hardness (3.02 GPa), compared to those (elastic modulus: 1.24 GPa, hardness: 0.05 GPa) for the film at 20 W. It was likely that the film with higher mechanical strength was not significantly affected by ion bombardments during etching process. When the film has higher mechanical properties, the effect of ion bombardments on the film may not be dominant. Fig. 3 (b) shows the refractive index of SiCOH thin films deposited at 20 and 100 W for the various etching gases. For the films deposited at 20 W, the refractive indices decreased slightly after etching from the value (1.446) of as-deposited film. In comparison, the refractive indices increased after etching from the value (1.515) of as-deposited film at 100 W. An increase in refractive index is expected to be correlated with less porosity, i.e., densification of the film, water adsorption, or a combination of both, and a higher *k*-values [47,48]. It was likely that the films at 100 W could bring an increased *k*-values after plasma etching based on the increased refractive index.

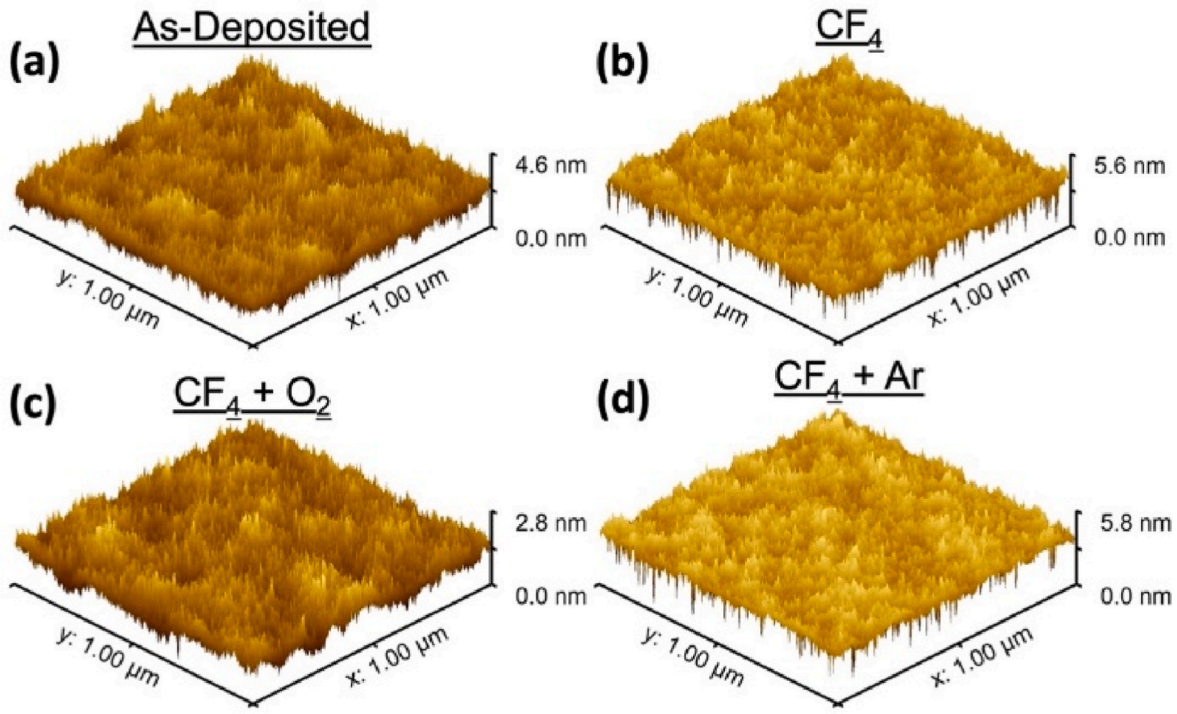

Fig. 4. AFM surface morphology of (a) as-deposited and etched SiCOH thin films using etching gases of (b) CF_4, (c) CF_4+O_2, and (d) CF_4+Ar for the deposition plasma power of 20 W.

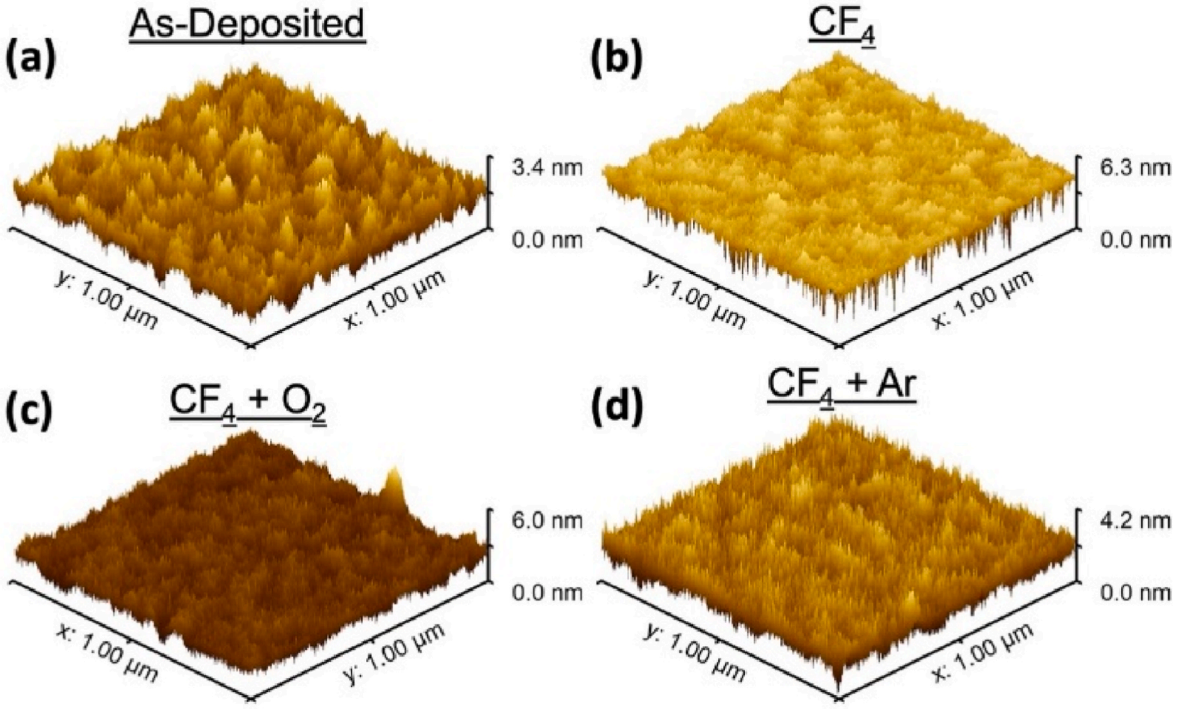

Fig. 5. AFM surface morphology of (a) as-deposited and etched SiCOH thin films using etching gases of (b) CF_4, (c) CF_4+O_2, and (d) CF_4+Ar for the deposition plasma power of 100 W.

3.3. Surface morphology

Fig. 4(a)–(d) show AFM surface morphology images of the as-deposited film and etched films in three etching conditions with CF_4, CF_4+O_2, and CF_4+Ar, respectively. All films were deposited at 20 W. All images represent an area of 1 µm × 1 µm of each sample. Scale bars on the right of each image indicate the difference between the highest peak and lowest trough of each sample area. The surface roughness depends on the film being etched and on the etch chemistry. The smallest range of the scale bar occurred for the film etched in CF_4+O_2 at 2.8 nm compared to ranges of 4.6 nm for the as-deposited film and 5.6–5.8 nm for the film etched in CF_4 or CF_4+Ar. Fig. 5(a)-(d) show AFM surface morphology

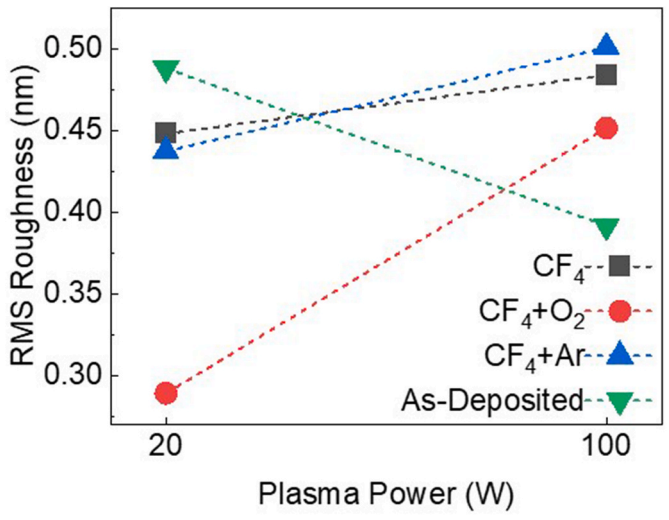

Fig. 6. Surface roughness of as-deposited and etched SiCOH thin films using etching gases of CF_4, CF_4+O_2, and CF_4+Ar for deposition plasma powers of 20 and 100 W.

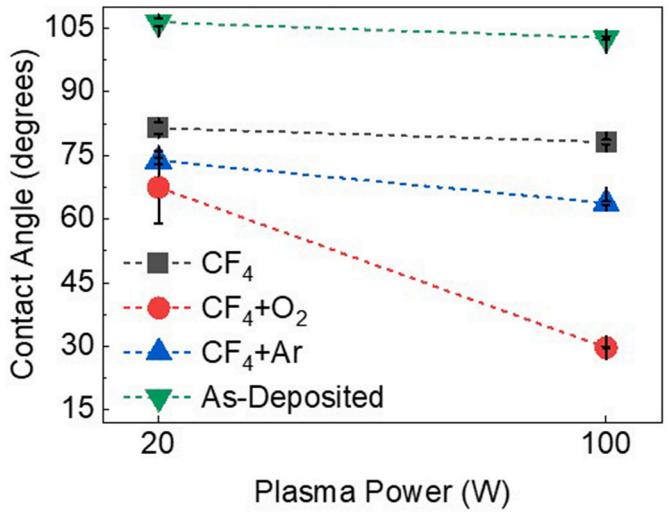

Fig. 7. Contact angles of as-deposited and etched SiCOH thin films using etching gases of CF_4, CF_4+O_2, and CF_4+Ar for deposition plasma powers of 20 and 100 W.

images of the as-deposited film and etched films in three etching conditions with CF_4, CF_4+O_2, and CF_4+Ar, respectively. All films were deposited at 100 W. From the images taken from the area of 1 μm × 1 μm of each sample, the ranges of the scale bars increased to 4.2–6.3 nm after etching from 3.4 nm for the as-deposited film.

Fig. 6 presents the RMS roughness values calculated for the as-deposited film and etched films under CF_4, CF_4+O_2, and CF_4+Ar gases. As-deposited SiCOH films showed a decrease in RMS roughness from 0.49 to 0.39 nm as the plasma power increased from 20 to 100 W. This difference can be associated with the density of films. It was likely that less dense structure in the film deposited at 20 W exhibited a higher surface roughness. After etching of the films deposited at 20 W, surface roughness decreased for all three etching conditions. Etching with CF_4+O_2 of the film deposited at 20 W showed the lowest surface roughness of 0.29 nm. However, the films deposited at 100 W showed increased surface roughness after etching with all three etching conditions. It was noted that etching in CF_4+O_2 produced the lowest surface roughness of 0.29 and 0.45 nm for the films at 20 and 100 W, respectively, among three etching conditions.

3.4. Contact angle measurement

Fig. 7 shows the contact angles for as-deposited and etched SiCOH thin films using etching gases of CF_4, CF_4+O_2, and CF_4+Ar. Deposition plasma powers were 20 and 100 W. Contact angles of as-deposited films at 20 and 100 W were 106.4 and 102.8°, respectively, which indicated both as-deposited films were hydrophobic. After etching, contact angles decreased below 90°, demonstrating the films became hydrophilic, regardless of deposition plasma power. This increase in hydrophilicity is expected to be associated with a decrease in methyl groups removed from plasma bombardment in addition to an increase in fluorine concentration [49]. Etching in CF_4+O_2 resulted in the smallest contact angle of 67.5° and 29.7° for the films deposited at 20 and 100 W, respectively. It appears that a more hydrophilic surface suggests the presence of oxygen on the thin film surface as a result of adding O_2 to CF_4 for etching. Although a considerable decrease in contact angle of the film at 100 W was observed for etching in CF_4+O_2, a little change in contact angles occurred between the films at 20 and 100 W when CF_4 was used for etching. When Ar was added to CF_4 for etching, the contact angle for the film at 20 W was measured at 73.8° while the film at 100 W showed the contact angle of 63.8°.

3.5. FTIR analysis

Chemical analysis was performed for as-deposited films as well as films after etching to study the chemical makeup of the film and the etching effects on them. Fig. 8(a) and (b) shows the FTIR spectra of as-deposited and etched films at deposition plasma powers of 20 and 100 W, respectively. Si–O and hydrocarbon related bonding were the dominant structures in the thin films. Four major peaks were identified as Si–O–Si stretching, Si–CH_3 bending, Si-$(CH_3)_x$ stretching, and CH_x stretching modes, corresponding to their respective wavenumbers of 1200–900, 1300–1200, 950–650, and 3000-2800 cm^{-1} [50]. For as-deposited films, Si–CH_3 bending mode was depressed as the plasma power increased from 20 to 100 W and the peak intensity of CH_x stretching mode was relatively lower than those of the rest of modes for both cases of 20 and 100 W. Si–O–Si stretching and Si-$(CH_3)_x$ stretching modes were overlapped at around 1000 cm^{-1} for as-deposited films but clearly separated after etching. Fig. 8(c) presents the peak area ratios for each of the four predominant peaks for the films deposited at 20 and 100 W before and after etching. Peak area ratios were calculated as the peak area of one peak divided by the sum of the peak areas of all four prominent peaks in the FTIR spectra. For the films deposited at 20 W, the Si–O–Si mode was dominant with peak area ratios in the range of 51.9–57.1% in all films, followed by Si-$(CH_3)_x$ mode with those in the range of 37.8–43.2%. Peak area ratios of Si–CH_3 and CH_x modes were relatively small below 10%. Etching in a sole CF_4 gas produced the largest fraction of Si–O–Si mode with 57% and the smallest fraction of Si-$(CH_3)_x$ mode with 38%, compared to as-deposited film and the other two etching conditions. For the films deposited at 100 W, a very similar trend in peak area ratios was observed as seen in the films at 20 W. The largest fraction of Si–O–Si mode with 69.2% and the smallest fraction of Si-$(CH_3)_x$ mode with 28.3% were obtained for etching in CF_4. Peak area ratios of Si–CH_3 and CH_x were below 4% which was even smaller than those of all etching conditions for the films at 20 W. After etching under three different gases, overall peak area ratios of Si–O–Si mode increased and those of Si-$(CH_3)_x$ decreased as the plasma power increased from 20 to 100 W. The films etched with CF_4+O_2 displayed smaller concentrations of Si–O–Si bonding compared to those etched in CF_4 or CF_4+Ar.

Fig. 9(a)-(c) shows the deconvolution of the Si–O–Si, Si–CH_3, and Si-$(CH_3)_x$ peaks for the films etched in CF_4, respectively. Graphs on the top for each figure are taken from the film deposited at 20 W and those on the bottom are the film deposited at 100 W. Si–O–Si peaks were deconvoluted into three peaks of cage, network, and suboxide structures, assigned at wavenumbers of 1135, 1063, 1023 cm^{-1}, respectively [6,51]. These three components are based on the Si–O–Si bonding angles

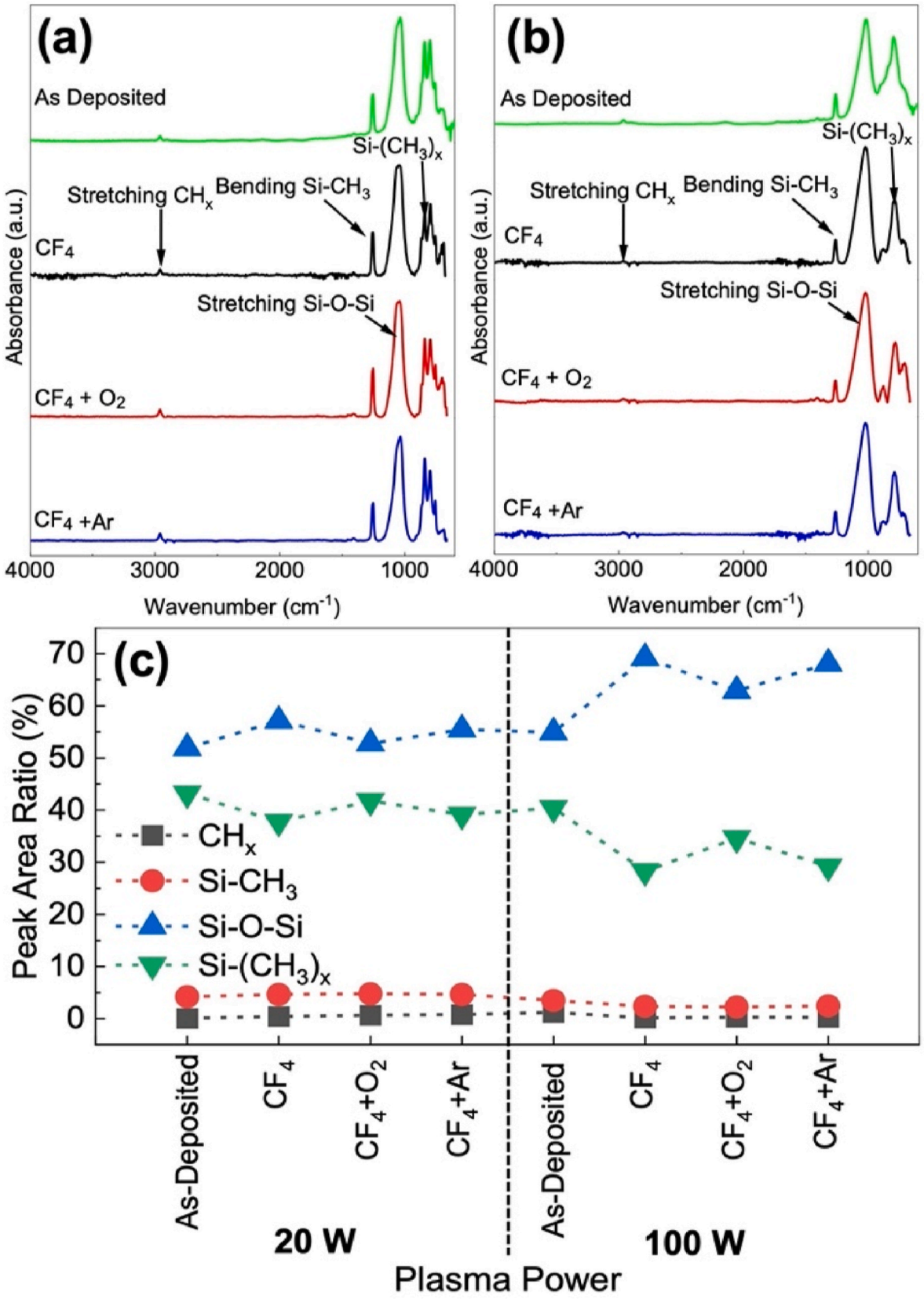

Fig. 8. FTIR spectra of as-deposited and etched SiCOH thin films at deposition plasma powers of (a) 20 W and (b) 100 W and (c) calculated peak area ratios of four prominent absorption bands. Etching gases were selected among CF_4, CF_4+O_2, and CF_4+Ar.

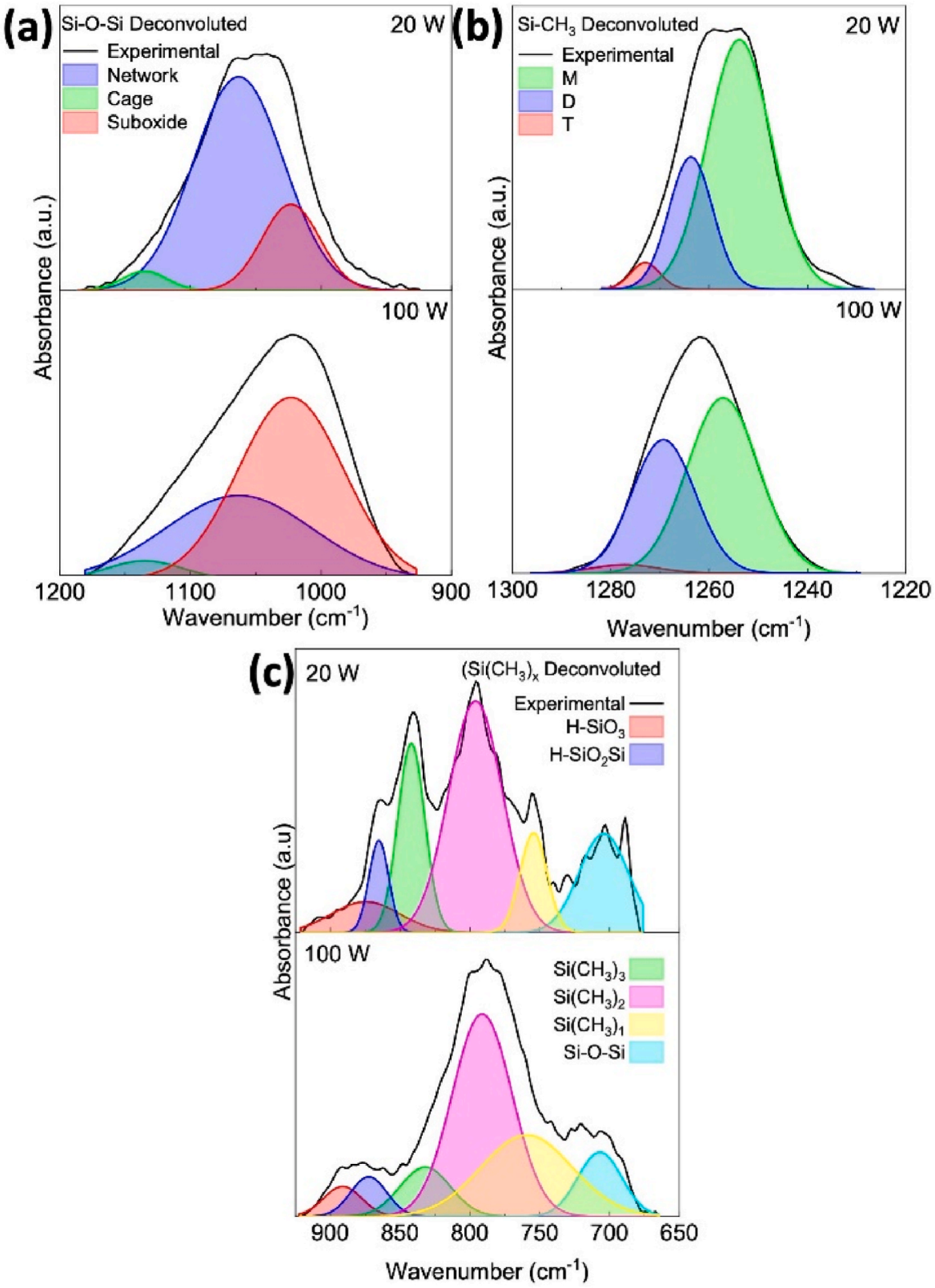

Fig. 9. Deconvolution of (a) Si–O–Si, (b) Si–CH_3, and (c) Si-$(CH_3)_x$ absorption bands for etched SiCOH thin films using CF_4. Plasma powers for the film deposition were 20 and 100 W, respectively.

of 150°, 140°, and less than 140° approximately for cage, network, and suboxide structures, respectively [6,51]. The fractions of peak areas of structures were different between the films at 20 and 100 W after etching with CF_4. The network structure had a large portion of Si–O–Si for the film at 20 W compared to a larger suboxide structure for the film at 100 W. Si–CH_3 peaks were deconvoluted into an M − , D-, and T-groups, representing OSi-$(CH_3)_3$ at 1254 cm^{-1}, O_2Si-$(CH_3)_2$ at 1262 cm^{-1}, and O_3Si–CH_3 at 1273 cm^{-1}, respectively [52]. These were

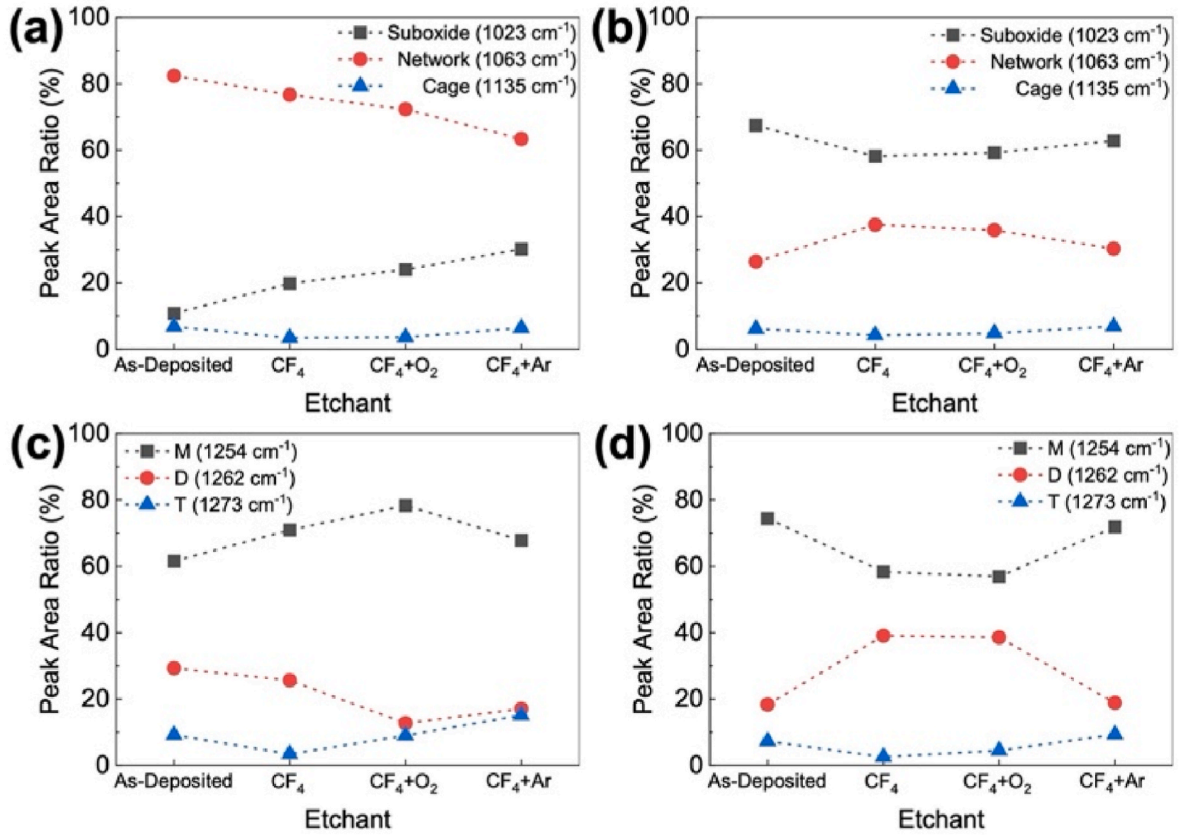

Fig. 10. Peak area ratios for deconvoluted absorption bands of Si–O–Si for etched SiCOH thin films for the deposition plasma powers of (a) 20 and (b) 100 W and Si–CH_3 for etched SiCOH thin films deposited at (c) 20 and (d) 100 W. Etching gases were selected among CF_4, CF_4+O_2, and CF_4+Ar.

denominated based on the bonding state of the silicon atom incorporated with the methyl groups. For example, three oxygen atoms and one methyl group are connected to a single silicon atom in the T-group. The fraction of D-group increased and those of M − and T-groups decreased as the plasma power increased from 20 to 100 W. Si-$(CH_3)_x$ peaks were deconvoluted to H–SiO_3, H–SiO_2Si, Si$(CH_3)_3$, Si$(CH_3)_2$, Si$(CH_3)_1$, and Si–O–Si modes, assigned at wavenumbers of 890, 865, 845, 802, 754, and 710 cm^{-1} [6,53]. The most prominent peak was Si$(CH_3)_2$ for both the films at 20 and 100 W. The fraction of Si$(CH_3)_3$ decreased but that of Si$(CH_3)_1$ increased as the plasma power increased from 20 to 100 W.

Fig. 10(a) and (b) presents peak area ratios for the deconvoluted absorption peaks of Si–O–Si stretching mode depending on etching

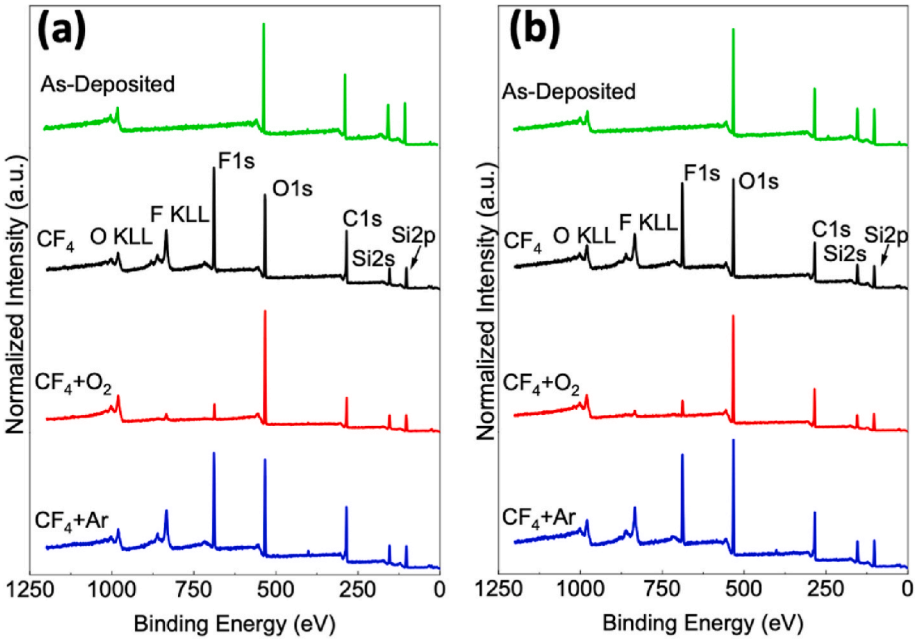

Fig. 11. XPS survey scans of as-deposited and etched SiCOH thin films using various etching gases for deposition plasma powers of (a) 20 and (b) 100 W.

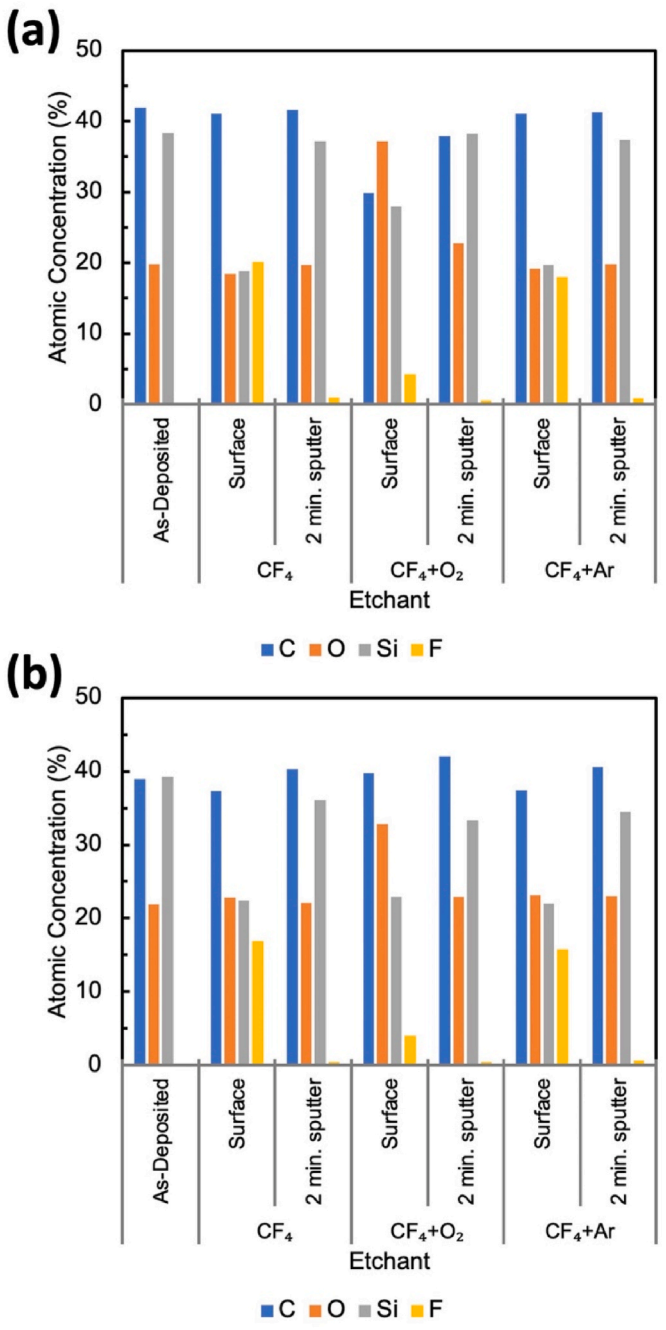

Fig. 12. Atomic concentrations of as-deposited and etched SiCOH thin films using various etching gases for deposition plasma powers of (a) 20 and (b) 100 W. Atomic concentrations of etched films were measured additionally after 2 min of Ar ion sputtering.

conditions for the films deposited at 20 and 100 W, respectively. For the films deposited at 20 W, the network Si–O–Si structure was still dominant after etching. The fraction of the network structure decreased from 82.4 to 76.7% when the film was etched in CF_4. When O_2 or Ar were added to CF_4 for etching, the fraction of the network structure further decreased to 72.3 or 63.4%, respectively. The fractions of the suboxide structure increased from 10.8 to 19.8% when the film was etched in CF_4. Additional etchant gases of O_2 or Ar to CF_4 resulted in an increase of the suboxide structure to 24.0 or 30.2%, respectively. For the films deposited at 100 W, the suboxide structure was dominant followed by the network and cage structures before and after etching. The fractions of the suboxide structure were in the range of 58.2–62.8% for all three etching conditions, lower than that of as-deposited film. For both 20 and 100 W cases, the fractions of cage structure were small, less than 6.2% without much change after etching in all three conditions. Fig. 10(c) and (d) represents peak area ratios for the deconvoluted absorption peaks of Si–CH_3 bonding configurations depending on etching conditions for the films deposited at 20 and 100 W, respectively. M-groups were dominant for both 20 and 100 W cases. For the films deposited at 20 W, the fraction of M-group increased but that of D-group decreased after etching. The highest fraction of M-group was obtained as 78.3% for etching in CF_4+O_2. For the films deposited at 100 W, the fraction of M-group decreased and that of D-group increased after etching. The largest fraction of D-group with 39.1% and smallest fraction of M-group with 56.9% were observed after etching in CF_4 and CF_4+O_2, respectively. The fraction of T-group was small, less than 9.3% for both 20 and 100 W cases.

3.6. XPS analysis

XPS analysis was used to study the chemical bonding configuration and atomic concentration on the surface of the SiCOH films before and after etching processes. Fig. 11(a) and (b) shows the survey scans for as-deposited and etched films in CF_4, CF_4+O_2, and CF_4+Ar for deposition plasma power of 20 and 100 W, respectively. Four prominent peaks were identified as C1s (284.8 eV), Si2p (~102 eV), F1s (~688 eV), and O1s (~533 eV) [54]. The peak of Si2s (~150 eV) was also present with a small intensity. The two "KLL" peaks were observed resulting from the exciting of Auger electron emission related to oxygen (~980 eV) and fluorine (~830 eV) [55]. F1s peak was clearly observed in the films after etching, as a result of the interaction between CF_4-based etching gas and the film. The intensities of Si2p and C1s peaks decreased after etching in CF_4 or CF_4+Ar and further decreased after etching in CF_4+O_2. The highest intensity of O1s peak was obtained for etching in CF_4+O_2. The intensity of the F1s peak for etching in CF_4 was similar to that in CF_4+Ar while the intensity of F1s peak remarkably decreased for etching in CF_4+O_2.

Fig. 12(a) and (b) shows atomic concentrations for as-deposited films at 20 and 100 W, as well as the films after etching with CF_4, CF_4+O_2, and CF_4+Ar. Atomic concentrations were calculated using the peak area ratios from four peaks presented in the XPS spectra. To investigate the change in elemental compositions through the depth of the film as well as the surface of the etched film, additional high-resolution scans for four prominent peaks were conducted after Ar ion sputtering for 2 min. Carbon concentration of the as-deposited film at 20 W was 41.9% whereas that of the as-deposited film at 100 W was 39.0%. Silicon concentrations were calculated as 38.3 and 39.2% for as-deposited films at 20 and 100 W, respectively. Oxygen concentrations were observed as 19.8 and 21.8% for as-deposited films at 20 and 100 W, respectively. After etching with three different gas mixtures, the concentration of silicon significantly decreased on the surface. Interestingly, oxygen concentrations drastically increased on the surface after etching in CF_4+O_2. Additionally, high fluorine concentrations were revealed on the surface of the films after etching. The films deposited at 20 W contained fluorine concentrations of 20.2 and 18.1% for etching in CF_4 and CF_4+Ar, respectively, and 4.3% for etching in CF_4+O_2. The films deposited at 100 W showed slightly lower fluorine concentrations of 16.9 and 15.8% for etching in CF_4 and CF_4+Ar, respectively, and 4.0% for etching in CF_4+O_2. Decreased silicon concentration on the surface recovered to the concentration of as-deposited films after 2 min of Ar sputtering. Fluorine was present but only in smaller concentrations (less than 1%) indicating fluorine implantation in the films after 2 min of Ar sputtering. It was likely that fluorine diffusion into the film occurred mostly at the surface. As previously mentioned, oxygen in the plasma interacts with CF_x radicals reducing the fluorine concentration on the surface of the films etched in CF_4+O_2. The films etched in CF_4+O_2 showed much higher oxygen concentrations on the surface. Oxygen concentrations were obtained as 37.2 and 32.9% for etching in CF_4+O_2,

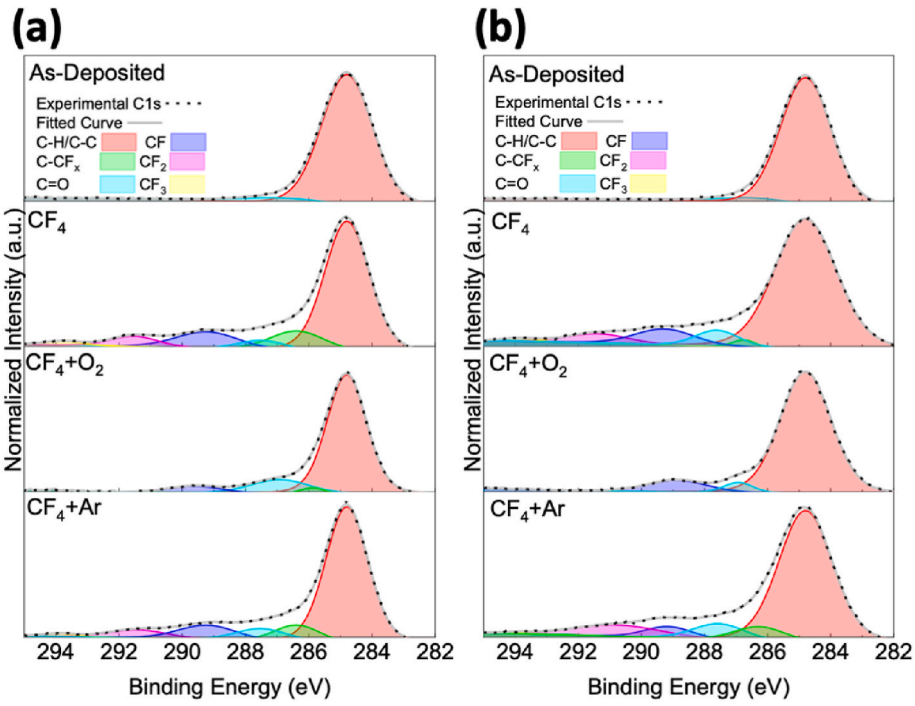

Fig. 13. Deconvolution of the C1s peaks for as-deposited and etched SiCOH thin films using various etching gases for deposition plasma powers of (a) 20 and (b) 100 W.

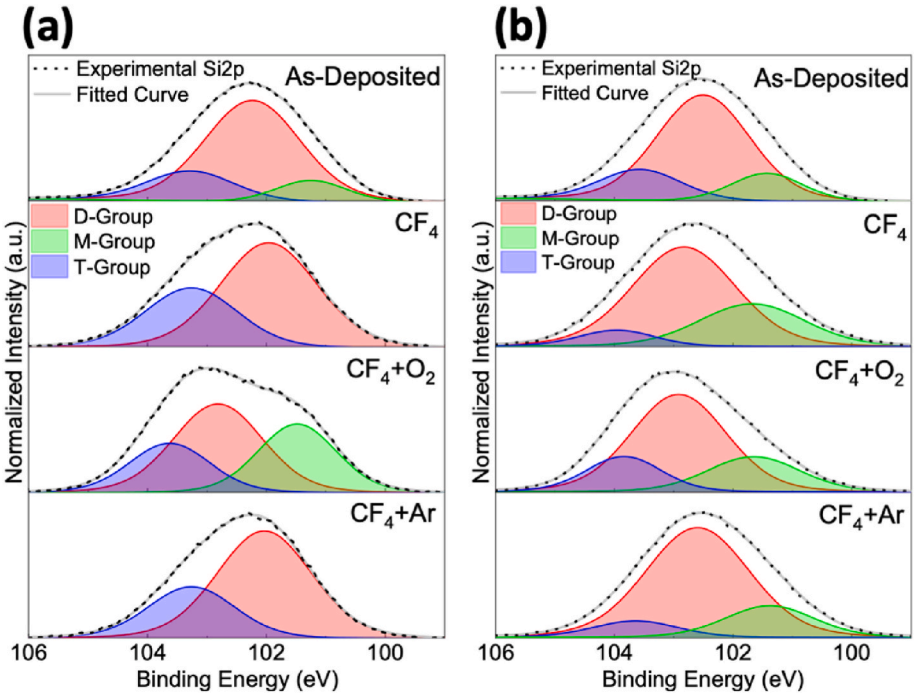

Fig. 14. Deconvolution of the Si2p peaks for as-deposited and etched SiCOH thin films using various etching gases for deposition plasma powers of (a) 20 and (b) 100 W.

compared to 18.4 and 22.8% for etching in CF_4 for deposition plasma powers at 20 and 100 W, respectively. It was probable that the depth or degree of plasma damage due to chemical effect was determined by the diffusion of radicals such as oxygen and fluorine into the film, especially through pores. Although the porosity was not directly measured, it was reasonable to infer that more pores were expected for the film at 20 W with a smaller refractive index. It was known that oxygen radicals deeply penetrate into the pores [20]. For etching in CF_4+O_2, a higher oxygen concentration of 37.2% for the film at 20 W was observed than the concentration of 32.9% for the film at 100 W due to more oxygen radicals penetrated through more pores of the film at 20 W. It was likely that oxygen radicals inhibited the penetration of fluorine radicals based on the observation that fluorine concentrations for the films at 20 and 100 W were 4.27 and 3.99%, respectively, which were much lower than

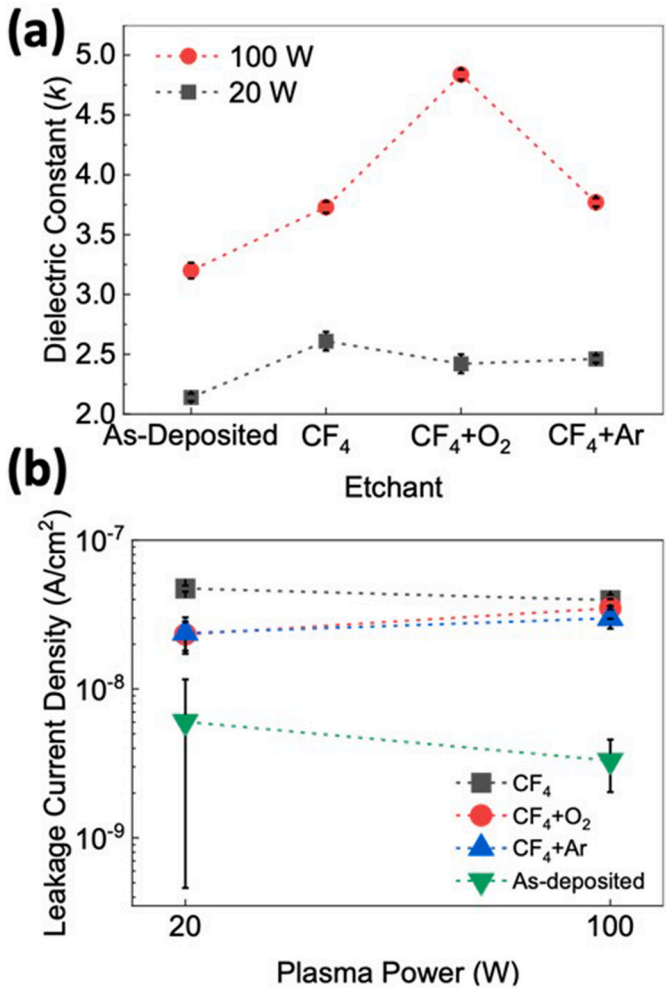

Fig. 15. (a) Dielectric constant (k) and (b) leakage current density of as-deposited and etched SiCOH thin films using various etching gases for deposition plasma powers of 20 and 100 W.

those for the films etched in CF_4 or CF_4+Ar. It was expected that additional gases such as O_2 and Ar to CF_4 in plasma processing could make more complex etching mechanism with chemical reaction and physical ion bombardment.

Fig. 13(a) and (b) shows the deconvolution of the C1s peaks for as-deposited and etched SiCOH thin films for deposition plasma powers of 20 and 100 W, respectively. The raw data and fitted curve are indicated by a black dotted line and a gray solid line, respectively. As-deposited films exhibited a prominent C–H/C–C peak at 284.8 eV with a small shoulder attributed to C═O bonding around 287 eV. Obviously, the films etched in CF_4 showed CF_x species, induced from fluorine bonded with carbon of the film. The films etched in CF_4 or CF_4+Ar were deconvoluted into six peaks corresponding to C–H/C–C, C-CF_x, C═O, C–F, C–F_2, and C–F_3, located at approximate binding energies of 284.8, 286.4, 287.6, 289.2, 291.4, and 293.8 eV, respectively [32,56]. The main peak was C–H/C–C for all thin films even after etching although its peak area ratio decreased as the films were etched with CF_4-containing gases. Both C–F_2 and C–F_3 peaks disappeared when the films were etched in CF_4+O_2.

Fig. 14(a) and (b) presents the deconvolution of the Si2p peaks for as-deposited and etched SiCOH thin films for deposition plasma powers of 20 and 100 W, respectively. The raw data and fitted curve are indicated by a black dotted line and a gray solid line, respectively. Each spectrum consisted of three peaks, M − , D-, and T-groups attributed to O–Si–C_3 (101.9 eV), O_2–Si–C_2 (102.9 eV), and O_3–Si–C (103.7 ± 0.1 eV) configurations, respectively [51]. For as-deposited films at 20 and 100 W, D-group was predominant with their respective peak area ratios of 69.9 and 68.3%. For the films deposited at 20 W, the M-group vanished for etching in CF_4 and CF_4+Ar whereas its peak area ratio increased for etching in CF_4+O_2. For the films deposited at 100 W, all three configurations were distributed with the largest peak area ratio of D-group followed by M − and T-groups after etching.

3.7. Dielectric constant and leakage current

Fig. 15(a) shows the dielectric constant of as-deposited and etched SiCOH thin films using various etching gases for deposition plasma powers of 20 and 100 W. The as-deposited film at 20 W showed a lower k-value of 2.14 compared to the value of 3.20 for the as-deposited film at 100 W. After etching, the k-values increased in the range of 2.42–2.61 for the films at 20 W. The k-values increased to 3.72–4.84 after etching for the films at 100 W. It was noted that the k-values were observed as the smallest increase with 13.1% and the largest increase with 51.1% from the k-values of as-deposited films at 20 and 100 W, respectively, for etching in CF_4+O_2. The increase in k-values could be explained by the fact that the layer was damaged by CF_4 and O_2-induced plasma and chemical compositions were modified on the surface and within the film during the etching process [57,58]. This is further confirmed through the increased hydrophilic nature discussed above. Interestingly, samples etched in CF_4+O_2 were the most hydrophilic and had the highest dielectric constant values. Fig. 15(b) shows the leakage current density of as-deposited and etched SiCOH thin films using various etching gases for deposition plasma powers of 20 and 100 W. As-deposited films at 20 and 100 W had leakage current densities of 6.04×10^{-9} and 3.3×10^{-9} A/cm^2, respectively. The film at 100 W showed a slightly lower leakage current density attributed to the sample's higher density [59]. After etching with CF_4, CF_4+O_2, or CF_4+Ar, the films deposited at 20 W showed increased leakage current density in the range of 2.3×10^{-8} - 4.7×10^{-8} A/cm^2. Similarly, after etching of the films deposited at 100 W, the leakage current density increased to the range of 3.0×10^{-8} - 4.0×10^{-8} A/cm^2. The as-deposited SiCOH films showed a hydrophobic surface. Chemical changes of the surface during plasma processing made the films hydrophilic. It was probable that water with a k-value of ~80 adsorbed in the film surface, especially porous structure, resulted in an increase in the k-values and leakage current. The SiCOH films at 100 W showed more hydrophilicity than those at 20 W and this leaded to more increase in k-values for the films at 100 W, even above that of SiO_2.

4. Summary and conclusions

The SiCOH thin films deposited at plasma powers of 20 and 100 W using PECVD with a single precursor, TTMSS, were used to investigate the etching characteristics under fluorocarbon-based gases including CF_4, CF_4+O_2, and CF_4+Ar. From characterization of the as deposited SiCOH thin films, the samples deposited at 20 W plasma power were found to be less dense then the samples deposited at 100 W providing a lower k-value but less mechanical strength. Interestingly, the films deposited at 100 W showed higher etch rate and surface roughness than the films at 20 W after etching. Films etched in CF_4+O_2 showed the highest etch rate for both films. The surface of the film became hydrophilic after etching, in comparison with the as-deposited film being hydrophobic. Calculation of peak area ratios of the four prominent peaks from FTIR analysis reveal a larger fraction of Si–O–Si bonding in the samples deposited at 100 W. After etching, the film at 20 W had a large network fraction of Si–O–Si compared to a prominent suboxide fraction for the film at 100 W. All etched films showed a significant fluorine concentration at the surface indicative of a fluorocarbon layer. Small concentrations of fluorine were present in the film after argon sputtering revealing fluorine implantation in the films. The k-values and leakage current densities were found to increase after etching due to plasma damage and the change in chemical compositions on the film surface.

From this study, it was likely that the etching chemistry strongly affected plasma damage to the SiCOH thin films. With an optimized etching gas composition and conditions, plasma damage could be minimized to prevent from the degradation of electrical properties for the integration of advanced interconnects in the IC chip manufacturing.

CRediT authorship contribution statement

Jacob Comeaux: Data curation, Formal analysis, Investigation, Validation, Visualization, Writing – original draft, Writing – review & editing. **William Wirth:** Visualization, Validation, Investigation, Formal analysis, Data curation. **Justin Courville:** Data curation, Validation, Visualization. **Nam-Wuk Baek:** Validation, Data curation. **Donggeun Jung:** Conceptualization, Resources. **Seonhee Jang:** Writing – review & editing, Writing – original draft, Supervision, Resources, Project administration, Methodology, Investigation, Funding acquisition, Conceptualization.

Declaration of competing interest

The authors declare that they have no known competing financial interests or personal relationships that could have appeared to influence the work reported in this paper.

Acknowledgments

This work was supported by the National Science Foundation under Grant No. CMMI-2026801. The authors would like to thank the Nanofabrication Facility at Louisiana State University for use of nanofabrication equipment.

References

[1] G. Dubois, W. Volksen, in: M.R. Baklanov, P.S. Ho, E. Zschech (Eds.), Advanced Interconnects for ULSI Technology, first ed., John Wiley & Sons, Ltd, Chichester, UK, 2012, pp. 3–33.
[2] P.A. Kohl, Annu. Rev. Chem. Biomol. Eng. 2 (2011) 379.
[3] L. Favennec, V. Jousseaume, G. Gerbaud, A. Zenasni, G. Passemard, J. Appl. Phys. 102 (2007), 064107.
[4] H. You, P. Mennell, M. Shoudy, D. Sil, D. Dorman, S. Cohen, E. Liniger, T. Shaw, T.-L. Leo, D. Canaperi, M. Raymond, A. Madan, A. Grill, J. Vac. Sci. Technol., B 36 (2018), 012202.
[5] V. Jousseaume, A. Zenasni, Olivier Gourhant, L. Favennec, in: M.R. Baklanov, P. Ho, E. Zschech (Eds.), Advanced Interconnects for ULSI Technology, Wiley, 2012.
[6] A. Grill, D.A. Neumayer, J. Appl. Phys. 94 (2003) 6697.
[7] S. Kwon, Y. Park, W. Ban, Y. Kim, J. Jang, D. Jung, J. Nanosci. Nanotechnol. 20 (2020) 2301.
[8] D. Priyadarshini, S.V. Nguyen, H. Shobha, E. Liniger, J.H.-C. Chen, H. Huang, S. A. Cohen, A. Grill, J. Vac. Sci. Technol., B 35 (2017), 021201.
[9] B.G. Streetman, S.K. Banerjee, Solid State Electronic Devices, sixth ed., Pearson College Div, 2006.
[10] M.R. Baklanov, C. Adelmann, L. Zhao, S. De Gendt, ECS J. Solid State ST. 4 (2015) Y1.
[11] M. Darnon, N. Casiez, T. Chevolleau, G. Dubois, W. Volksen, T.J. Frot, R. Hurand, T.L. David, N. Posseme, N. Rochat, C. Licitra, J. Vac. Sci. Technol., B 31 (2013), 011207.
[12] Y.-L. Cheng, C.-Y. Lee, C.-W. Haung, in: H. Jelassi, D. Benredjem, IntechOpen (Eds.), Plasma Science and Technology - Basic Fundamentals and Modern Applications, 2019.
[13] B.R. Rogers, T.S. Cale, Vacuum 65 (2002) 267.
[14] M. Kalisz, R.B. Beck, M. Ćwil, Vacuum 82 (2008) 1046.
[15] T.V. Rakhimova, D.V. Lopaev, Y.A. Mankelevich, K.A. Kurchikov, S.M. Zyryanov, A.P. Palov, O.V. Proshina, K.I. Maslakov, M.R. Baklanov, J. Phys. D Appl. Phys. 48 (2015), 175204.
[16] N. Posseme, T. Chevolleau, O. Joubert, L. Vallier, N. Rochat, J. Vac. Sci. Technol., B 22 (2004) 2772.
[17] H.W. Tak, J.K. Jang, D. Sung, D.S. Kim, D.W. Kim, G.Y. Yeom, Mat. Express 10 (2020) 834.
[18] C. Cardinaud, G. Turban, Appl. Surf. Sci. 45 (1990) 109.
[19] T.E.F.M. Standaert, P.J. Matsuo, S.D. Allen, G.S. Oehrlein, T.J. Dalton, J. Vac. Sci. Technol., A 17 (1999) 741.
[20] M.R. Baklanov, J.-F. de Marneffe, D. Shamiryan, A.M. Urbanowicz, H. Shi, T. V. Rakhimova, H. Huang, P.S. Ho, J. Appl. Phys. 113 (2013), 041101.
[21] E.T. Ryan, S.M. Gates, A. Grill, S. Molis, P. Flaitz, J. Arnold, M. Sankarapandian, S. A. Cohen, Y. Ostrovski, C. Dimitrakopoulos, J. Appl. Phys. 104 (2008), 094109.
[22] J.J. Bao, H. Shi, J. Liu, H. Huang, P.S. Ho, M.D. Goodner, M. Moinpour, G. M. Kloster, J. Vac. Sci. Technol., B 26 (2008) 9.
[23] I. Chun, A. Efremov, G.Y. Yeom, K.-H. Kwon, Thin Solid Films 579 (2015) 136.
[24] J. Lee, A. Efremov, K.-H. Kwon, Vacuum 148 (2018) 214.
[25] V. McGahay, Materials 3 (2010) 536.
[26] M.R. Baklanov, Q.T. Le, E. Kesters, F. Iacopi, J. Van Aelst, H. Struyf, W. Boullart, Vanhaelemeersch, K. Maex, in: Proceedings of the IEEE 2004 International Interconnect Technology Conference, IEEE, Burlingame, CA, USA, 2004, pp. 187–189 (IEEE Cat. No.04TH8729).
[27] H.F. Winters, J.W. Coburn, Surf. Sci. Rep. 14 (1992) 162.
[28] V.V. Smirnov, A.V. Stengach, K.G. Gaynullin, V.A. Pavlovsky, S. Rauf, P.L. G. Ventzek, J. Appl. Phys. 101 (2007), 053307.
[29] H. Miyajima, H. Masuda, K. Watanabe, K. Ishikawa, M. Sekine, M. Hori, Micro Nano Eng. 3 (2019) 1.
[30] M.V.V.S. Rao, S.P. Sharma, B.A. Cruden, M. Meyyappan, Plasma Sources Sci. Technol. 11 (2002) 69.
[31] A. Zotovich, O. Proshina, Z. el Otell, D. Lopaev, T. Rakhimova, A. Rakhimov, J.-F. de Marneffe, M.R. Baklanov, Plasma Sources Sci. Technol. 25 (2016), 055001.
[32] S. Lee, J. Woo, D. Jung, J. Yang, J. Boo, H. Kim, H. Chae, Thin Solid Films 517 (2009) 3942.
[33] H. Kim, M.H. Ha, D. Jung, H. Chae, H. Kim, Mater. Res. Bull. 47 (2012) 3008.
[34] C.-Y. Lee, Y.-H. Joo, M.P. Kim, D.-S. Um, C.-I. Kim, Coatings 11 (2021) 906.
[35] X. Guo, S.W. King, H. Zheng, P. Xue, Y. Nishi, J.L. Shohet, Appl. Phys. Lett. 106 (2015), 012904.
[36] X. Guo, H. Zheng, S.W. King, V.V. Afanas'ev, M.R. Baklanov, J.-F. de Marneffe, Y. Nishi, J.L. Shohet, Appl. Phys. Lett. 107 (2015), 082903.
[37] X. Guo, D. Pei, H. Zheng, W. Li, J.L. Shohet, S.W. King, Y.-H. Lin, H.-S. Fung, C.-C. Chen, Y. Nishi, J. Vac. Sci. Technol., A 35 (2017), 021509.
[38] J.W. DuMont, A.E. Marquardt, A.M. Cano, S.M. George, ACS Appl. Mater. Interfaces 9 (2017) 10296.
[39] X. Sun, T. Ma, D. Yin, B. Tan, F. Yang, M. Liu, P. Gao, S. Zhang, Y. Wang, Y. He, ECS J. Solid State Sci. Technol. 10 (2021), 024003.
[40] G. Greczynski, L. Hultman, ChemPhysChem 18 (2017) 1507.
[41] G. Greczynski, L. Hultman, Appl. Surf. Sci. 451 (2018) 99.
[42] G. Greczynski, L. Hultman, Angew. Chem. 132 (2020) 5034.
[43] C. Cardinaud, C. R. Chimie 21, 723 (2018).
[44] K. Lionti, W. Volksen, T. Magbitang, M. Darnon, G. Dubois, ECS J. Solid State Sci. Technol. 4 (2015) N3071.
[45] Y. Sun, M. Krishtab, H. Struyf, P. Verdonck, S. De Feyter, M.R. Baklanov, S. Armini, Langmuir 30 (2014) 3832.
[46] X. Guo, J.E. Jakes, S. Banna, Y. Nishi, J.L. Shohet, J. Appl. Phys. 116 (2014), 044103.
[47] E. Kunnen, M.R. Baklanov, A. Franquet, D. Shamiryan, T.V. Rakhimova, A. M. Urbanowicz, H. Struyf, W. Boullart, J. Vac. Sci. Technol., B 28 (2010) 450.
[4][8] S.-K. Kwak, K.-H. Jeong, S.-W. Rhee, J. Electrochem. Soc. 151 (2004) F11.
[49] H. Shi, J. Liu, H. Huang, P.S. Ho, M.D. Goodner, M. Moinpour, G.M. Kloster, J. Vac. Sci. Technol., B 26 (2008) 9.
[50] D. Kim, H. Kim, H. Jang, D. Jung, H. Chae, J. Nanosci. Nanotechnol. 12 (2012) 6040.
[51] Z.-J. Ding, Y.-P. Wang, W.-J. Liu, S.-J. Ding, M.R. Baklanov, D.W. Zhang, J. Phys. D Appl. Phys. 51 (2018), 115103.
[52] C.-H. Lo, M.-H. Lin, K.-S. Liao, M. De Guzman, H.-A. Tsai, V. Rouessac, T.-C. Wei, K.-R. Lee, J.-Y. Lai, J. Membr. Sci. 365 (2010) 418.
[53] Y. Park, H. Lim, S. Kwon, W. Ban, S. Jang, D. Jung, Thin Solid Films 727 (2021), 138680.
[54] J. Pereira, L.E. Pichon, R. Dussart, C. Cardinaud, C.Y. Duluard, E.H. Oubensaid, P. Lefaucheux, M. Boufnichel, P. Ranson, Appl. Phys. Lett. 94 (2009), 071501.
[55] J.F. Moulder, W.F. Stickle, P.E. Sobol, K.D. Bomben, J. Chastain, R.C. King Jr., in: Handbook of X-Ray Photoelectron Spectroscopy: A Reference Book of Standard Spectra for Identification and Interpretation of XPS Data (Physical Electronics, Eden Prairie, Minn., 1995. Physical Electronics, Incorporation.
[56] H. Jang, H. Kim, S. Lee, H. Moon, D. Jung, H. Chae, Nanosci. Nanotechnol. Lett. 9 (2017) 174.
[57] S. Zimmermann, N. Ahner, F. Blaschta, M. Schaller, H. Zimmermann, H. Rülke, N. Lang, J. Röpcke, S.E. Schulz, T. Gessner, Microelectron. Eng. 88 (2011) 671.
[58] O.V. Braginsky, A.S. Kovalev, D.V. Lopaev, E.M. Malykhin, YuA. Mankelevich, T. V. Rakhimova, A.T. Rakhimov, A.N. Vasilieva, S.M. Zyryanov, M.R. Baklanov, J. Appl. Phys. 108 (2010), 073303.
[59] Y. Lee, W. Ban, S. Jang, D. Jung, J. Nanosci. Nanotechnol. 21 (2021) 2139.